ORIGINAL RESEARCH PAPERS

On the interception of the optimal imaging plane for pleural line scanning with automatic robot assisted lung ultrasound: an experimental study

FEDERICO MENTO, LIBERTARIO DEMI

Department of Information Engineering and Computer Science, University of Trento, Trento, Italy

ABSTRACT

Background: Lung ultrasound (LUS) is nowadays an important tool to evaluate the state of lung surface. However, it is strongly operator-dependent, leading to reduced reproducibility of LUS analysis. Even though LUS acquisition protocols can improve LUS reproducibility and help standardizing LUS exams, human operators can guarantee only a limited precision in intercepting the optimal imaging plane. Hence, in this study, we assess the possibility to automatically intercept the optimal imaging plane in LUS examinations, i.e., the imaging plane perpendicular to the pleural plane (PP), by extracting three features, then utilized to guide a UR5e robotic arm handling an ultrasound probe.

Methods: The main focus of this study consists on evaluating the potential of these three features in estimating the PP position with respect to the probe. To do so, we designed a simplified but highly controllable environment, where PP was mimicked with a steel plate (to simulate a highly reflective acoustic interface), while intercostal tissues were mimicked with a 2-cm-thick beef meat. The environment was imaged with a linear probe connected to an ULA-OP platform, which was held by an UR5e, programmed to explore 8 different paths of acquisitions with a rotational angle (RA) ranging from −20° to 20° (1° step size). This resulted in 328 positions that could be explored; each position with RA=0° corresponds to the optimal imaging plane. Radiofrequency data were acquired and post-processed to form normalized log-scale B-Mode images. A rectangular region of interest, defined to include PP, was considered to compute mean intensity at each depth of the region of interest, along lateral dimension. Mean intensity as a function of depth was then utilized to extract three different features, then fed to genetic algorithms to solve optimization problems to guide UR5e towards the optimal imaging plane.

Received: 25 November 2025 | Accepted: 25 December 2025

Correspondence: Federico Mento, PhD / Via Sommarive 5, Trento (CAP 38123), Italy / E-mail: federico.mento@unitn.it

Results and Conclusions: Genetic algorithms converged towards an average error < 1° after exploring only 18 positions, showing strong potential in automatic probe placement for LUS.

Key words: Lung ultrasound (LUS), Pleural line (PL), Pleural plane (PP), Robot-Assisted Ultrasound.

Background

Lung ultrasound (LUS) is an important tool to assess the state of the lung surface, but it is strongly operator-dependent (1–3), thus leading to a reduced reproducibility of LUS analysis (4,5). This reproducibility can be improved by properly designing and adopting LUS acquisition protocols, which can also help standardizing LUS exams (4–6). Despite the use of standardized LUS acquisition protocols, human operators (HOs) can guarantee only a limited precision in intercepting the optimal imaging plane (O-ImP), i.e., *"the imaging plane (ImP) perpendicular to the pleural plane (PP)"*. Figure 1 clarifies how the intersection between the PP and the ImP is represented as the pleural line (PL) in the reconstructed B-Mode images.

Given the HOs' limited precision in intercepting the O-ImP in LUS examinations, we here propose an experimental study to assess the possibility to automatically intercept the O-ImP in LUS exams. Specifically, in this study, we introduce three features extracted from radiofrequency (RF) ultrasound signals to be utilized to guide a UR5e robotic arm (Universal Robots, Odense, Denmark) handling an ultrasound probe towards the O-ImP. These specific features are chosen to exploit both the high acoustic reflectivity of PL and its geometric property to be approximated, at least locally, to a straight line. To reach this goal, we have designed a highly controllable environment where we can physically guarantee the probe aperture, which can be seen as a plane defining the elevation and lateral dimensions, to be parallel to the PP, and, thus, the ImP to be perpendicular to the PP. Then, the knowledge of the angle between ImP and PP can be utilized as ground truth to assess the potential of the three investigated features in automatically intercepting the O-ImP.

To the authors' knowledge, no studies on robot-assisted LUS focused on the use of highly controlled experimental models to evaluate the capability of specific ultrasound features in characterizing the O-ImP. In contrast, previous studies mainly focused on automatically placing the ultrasound probe parallel to the body surface to maximize acoustic matching (7,8). Only a recent study on robot-assisted LUS (Lei *et al.* (9)) presented a strategy to optimize the probe placement based on its position with respect to the PP. Specifically, Lei *et al.* utilized the PL in the observed B-Mode image as a feedback to adjust the position of the probe to maintain the alignment of the PL with the lateral dimension of the image (9). Even though this strategy can provide advantages when applied for a specific direction of rotation of the probe aperture with respect to the PP, i.e., the one along the lateral dimension, it does not guarantee the interception of the O-ImP. Indeed, besides the direction of rotation along the lateral dimension, other directions of rotation exist. In addition, contrary to what we propose in our study, Lei *et al.* did not rely on ultrasound features validated on an experimental model in which the orthogonality of the ImP with respect to the PP is physically guaranteed. Specifically, in our study, we propose three new ultrasound features that correlate with the orthogonality of the ImP with respect to the PP, and could thus be utilized to automatically intercept the O-ImP in LUS examinations.

The rest of the paper is organized as follows. In the "Materials and Methods" section, the experimental environment and the data acquisition process will be presented. Then, the features' extraction procedure will be described and, finally, the genetic algorithms (GAs) used to solve the optimization problems aiming at guiding the UR5e robotic arm towards the O-ImP will

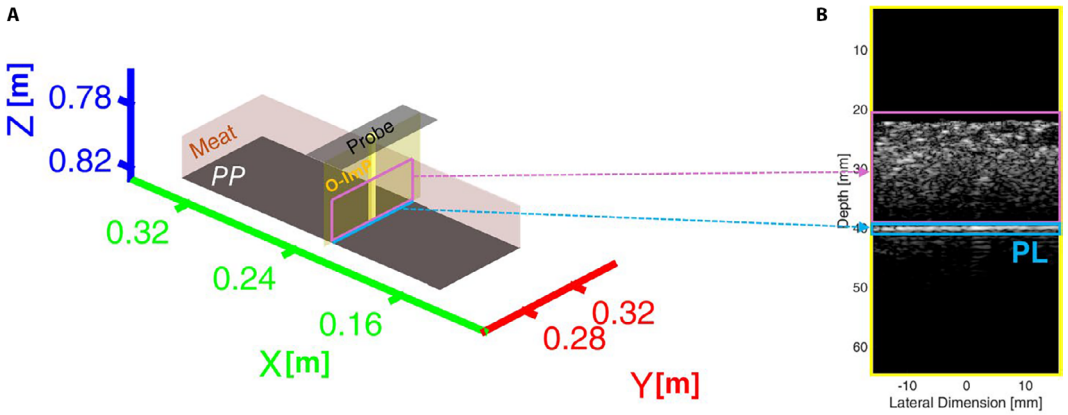

Figure 1. (A) An illustration of a LUS acquisition scenario is shown with (B) the corresponding reconstructed B-Mode image. It is important to observe how the intersection between PP and ImP (in this case, the O-ImP) is represented as the pleural line (PL) in the reconstructed B-Mode image.

be presented. The "Results" section will be dedicated to the quantitative results, whereas both discussion and conclusions will be provided in the last section ("Discussion and Conclusions").

Materials and methods

Experimental environment

In this study, a highly controllable environment (called ENV_{meat}) was designed by mimicking the PP with a flat steel plate having dimensions of 17 by 5 cm along X and Y dimensions, respectively (Figure 2). The plate is composed of austenitic stainless steel AISI (American Iron and Steel Institute) 316L (Euronorm number = 1.4404), and its flat surface has an arithmetic mean roughness smaller than 5 μm. Intercostal tissues were mimicked including a 2-cm-thick beef meat, which was placed on top of the steel plate. The steel plate was utilized to simulate a highly reflective acoustic interface, which is an acoustic property shared with the tissue/air acoustic interface present in real cases scenarios with aerated lungs. Indeed, a tissue/steel acoustic interface has the absolute value of the reflection coefficient $|R| \approx 0.93$, and a tissue/air acoustic interface has $|R| \approx 0.99$ (10). These similar values of $|R|$ are translated into a comparable percentage of energy reflected by these two acoustic interfaces. Moreover, we choose to utilize a flat steel plate rather than other models (as the sponge phantom presented by Blüthgen *et al.* (11)) as it guarantees a significantly high control in the experimental design, which cannot be guaranteed by the other models. Consistently, to validate the effectiveness of the proposed features, we required to have a flat surface. Moreover, even though the acoustic impedances of air and steel are significantly different (3.9×10^{-4} and 46.69 MRayl, respectively), following the Snell law, the $|R|$ values of tissue/air and tissue/steel acoustic interfaces remain comparable. As the high reflectivity was the property we were interested in, we opted to use a steel plate to mimic PP. Both steel plate and meat were then immersed in water to be imaged with a LA533 linear array probe (Esaote, Florence, Italy) [the probe's pitch and element size along the lateral dimension are respectively equal to 245 and 220 μm (12)] connected to an ULA-OP platform (13). An UR5e manipulator was utilized to held the probe and move it within a 3D volume defined by the X, Y, and Z spatial dimensions (Figure 2). As shown in Figure 3, the UR5e was programmed to explore 8 different acquisition paths, which could intercept different ImPs with rotational angles (RAs) ranging from –20° to 20° (1° step size). These 8 acquisition paths were defined as follows:

Path 1. lateral dimension of the probe (i.e., the longer one) oriented along the X axis, and both rotation and translation movements along the X axis;

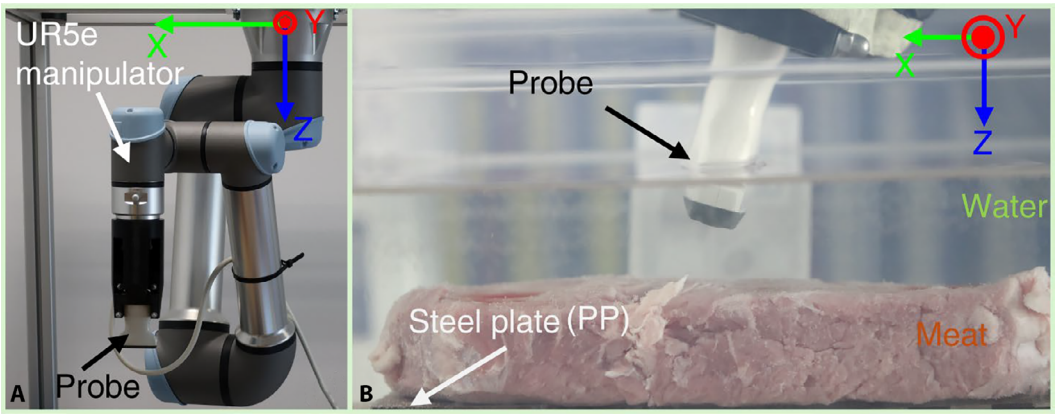

Figure 2. Experimental setup. (A) Picture of the UR5e robotic arm, handling the LA533 Esaote linear array probe. (B) Picture of the LA533 Esaote linear array probe immersed in water to image the meat and the steel plate (PP). The reference spatial coordinates X, Y, Z utilized to move the robot are also shown.

Path 2. lateral dimension of the probe (i.e., the longer one) oriented along the X axis, and both rotation and translation movements along the Y axis;

Path 3. lateral dimension of the probe (i.e., the longer one) oriented along the Y axis, and both rotation and translation movements along the Y axis;

Path 4. lateral dimension of the probe (i.e., the longer one) oriented along the Y axis, and both rotation and translation movements along the X axis;

Path 5. lateral dimension of the probe (i.e., the longer one) oriented along the X axis, and rotation movement along the X axis;

Path 6. lateral dimension of the probe (i.e., the longer one) oriented along the X axis, and rotation movement along the Y axis;

Path 7. lateral dimension of the probe (i.e., the longer one) oriented along the Y axis, and rotation movement along the Y axis;

Path 8. lateral dimension of the probe (i.e., the longer one) oriented along the Y axis, and rotation movement along the X axis.

To further clarify, we here intend as *"both rotation and translation movements"* the application of a rotation (along a specific dimension) combined with a translation aiming at guaranteeing a specific property to be maintained. Specifically, this combination of rotation and translation movements guarantees that the intersection between the imaginary line lying inside the ImP and connecting the center of the probe with the PP remains the same (see the yellow lines drawn in Figure 3 for *Paths 1*, *2*, *3*, and *4*). As clearly observable from Figure 3 (*Paths 5*, *6*, *7*, and *8*), this property is not maintained when only a rotation movement is applied. The total number of positions to be possibly explored by the UR5e is determined by the number of positions explorable in each acquisition path (i.e., 41, as RA ranges from -20° to 20° with a 1° step size) multiplied by the total number of acquisition paths (i.e., 8). Therefore, a total of 328 positions (*pos*) could be possibly explored. As each *pos* with RA=0° corresponds to an O-ImP, the UR5e could intercept 8 O-ImPs, among the 328 *pos* that could be explored.

Data acquisition parameters

To acquire RF data, for each transmission/reception event, a modulated pulse having center frequency equal to 6 MHz and a -6-dB bandwidth ≈ 4 MHz was transmitted. These specific center frequency and bandwidth were chosen both to properly cover the transfer function of the probe (-6-dB bandwidth from 3.8 to

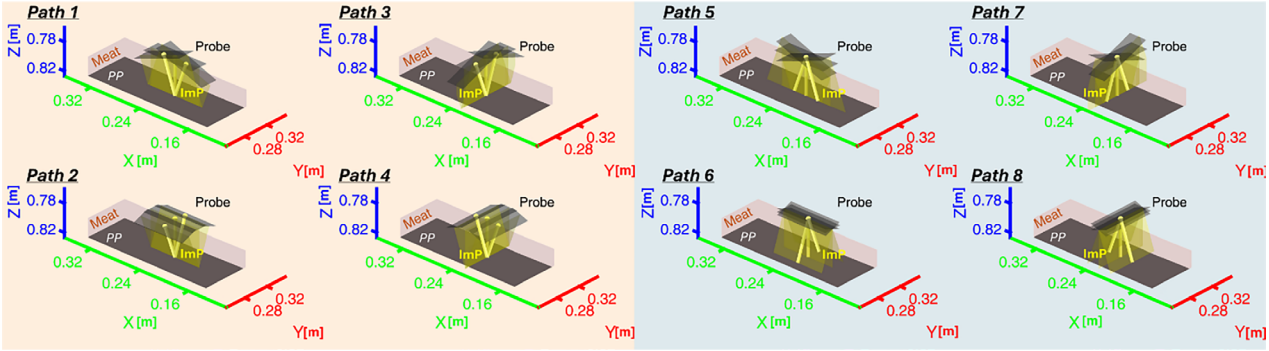

Figure 3. An illustration of the 8 different acquisition paths is shown. Each acquisition path consists of 41 different positions, with RA ranging from -20° to 20° (with a 1° step size). To simplify the visualization, for each acquisition path, we only depicted the ImP with RA = [-20°, 0°, 20°]. The 8 ImPs perpendicular to PP (i.e., the ones with RA = 0°) are the O-ImPs. Acquisition paths going from 1 to 4 consists of a combination of rotation and translation movements, whereas acquisition paths going from 5 to 8 consists of only a rotation movement. For each path and RA, the yellow line represents the imaginary line lying inside the ImP that connects the center of the probe with the PP. The reference spatial coordinates X, Y, Z are also shown.

12 MHz (12,14)) and limit attenuation phenomena occurring inside meat; indeed, a higher center frequency would translate in higher attenuation. For each transmission/reception event, we utilized a sub-aperture of 64 elements, corresponding to the maximum number of elements that can be controlled simultaneously by the ULA-OP (13). To avoid saturation phenomena at the PL, the pressure output was kept low by properly setting the transmitted pulse's amplitude. To reconstruct the images, dynamic focusing was applied in reception, whereas no focusing was utilized in transmission. No steering was applied in both transmission and reception phases. The post-beamformed images were reconstructed by linearly shifting the 64-elements sub-aperture over the entire array, composed of 192 elements. As a result, the reconstructed images consisted of 129 lines along the lateral dimension. The received signals were sampled with a 50-MHz sampling frequency, and a speed of sound of 1540 m/s was assumed for time to space conversion along depth dimension. Figure 4 shows examples of reconstructed log-scale B-Mode images for the 8 different acquisition paths as a function of RA (ranging from -20° to 20° with a 10°-step size). It is noticeable how at the shallowest depths of the images, i.e., up to approximately 20 mm, depending on the RA, the intensity values are significantly lower (depicted as black-colored pixels). Indeed, the shallowest part of the images is simply a reconstruction of the imaging area where only water is present. The post-processing operations applied to the RF data to form the normalized log-scale B-Mode images are described in the next section.

Features' extraction

Figure 5 shows how, after the acquisition, to form normalized log-scale B-Mode images, RF data were post-processed by sequentially applying

i. a 12th-order band-pass Butterworth filter (having a 6-MHz center frequency and a 4-MHz bandwidth),
ii. a Hilbert transform (to extract the envelope),
iii. log-scaling,
iv. normalization with respect to the maximum value.

Then, after forming the normalized log-scale B-Mode images, we selected a rectangular region of interest (ROI), defined to entirely include the PL. Specifically, the ROI is always defined as the region covering depths from 3 to 6 cm and including the entire lateral dimension. Afterwards, the mean intensity (MeIn) was computed at each depth of the ROI (along the lateral dimension). Thus, we mathematically defined MeIn, at a specific depth d inside the ROI, as follows:

$$- \quad \mathrm{MeIn}(d) = \sum_{l=1}^{129} \frac{intensity_{dBScale}(l,d)}{129},$$

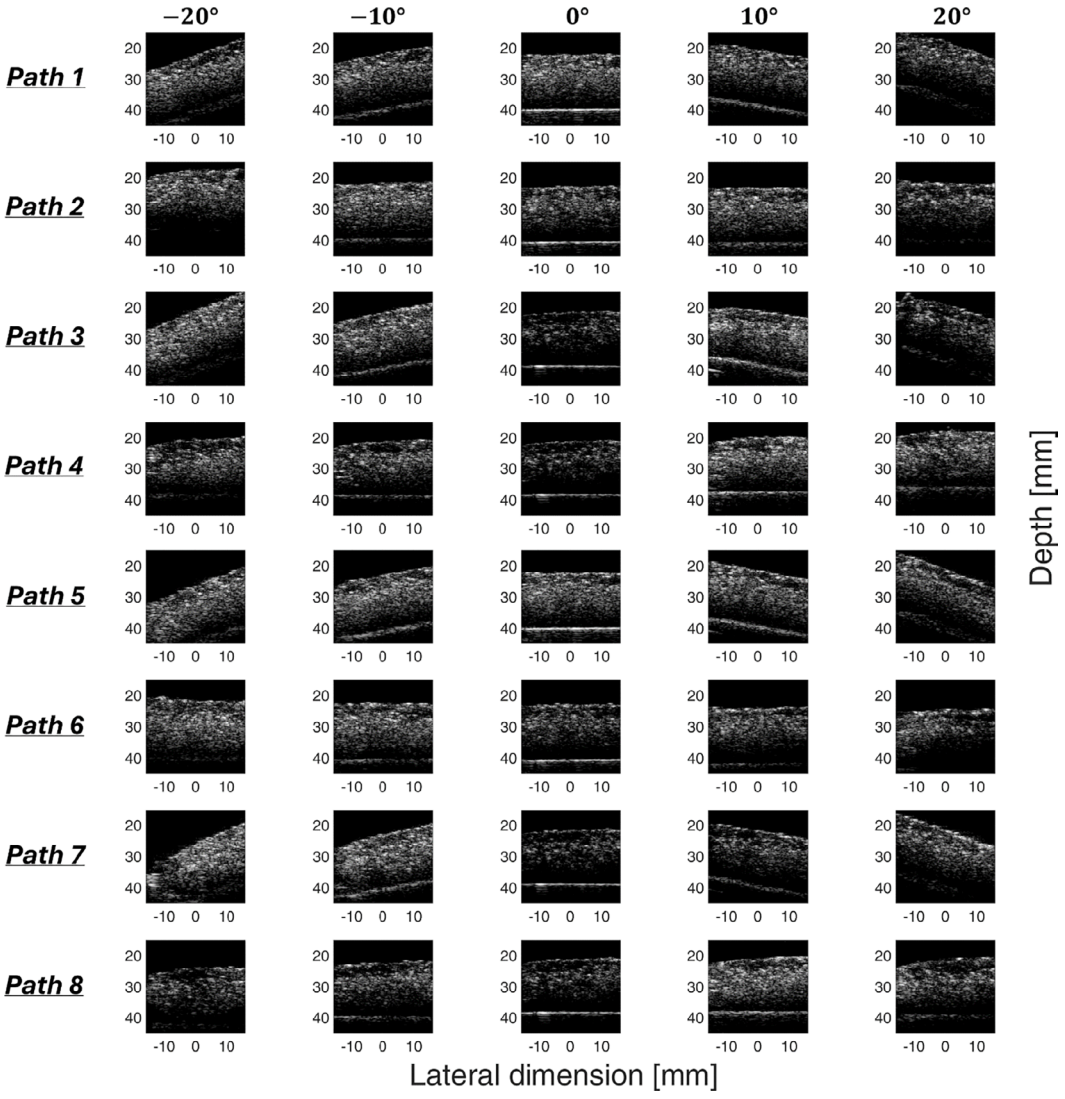

Figure 4. Examples of reconstructed log-scale B-Mode images for the 8 different acquisition paths as a function of RA (ranging from −20° to 20° with a 10°-step size). To improve visualization, the images are zoomed and displayed with an imaging depth ranging from 15 to 45 mm.

where l is an index numbering the 129 lines of the normalized log-scale B-Mode image along the lateral dimension and $intensity_{dBScale}(l,d)$ is the intensity value of the pixel at line l and depth d of the normalized log-scale B-Mode image.

MeIn as a function of depth was finally utilized to extract the three new ultrasound features, i.e.,

- f_1 = maximum of cross-correlation of MeIn with the envelope of the transmitted pulse (computed in linear scale);
- f_2 = variance of MeIn values;
- f_3 = spatial -12-dB-width of MeIn.

The specific operations performed to extract f_1, f_2, and f_3 are visually described with an example in Figure 6. Specifically, to extract f_1 from an input signal (MeIn), the following operations were performed: (i) both the MeIn and the transmitted pulse envelope were converted in linear scale (conversion performed as $intensity_{LinearScale} = 10^{intensity_{dBScale}}$, where $intensity_{LinearScale}$ and $intensity_{dBScale}$ are the intensity values in linear scale

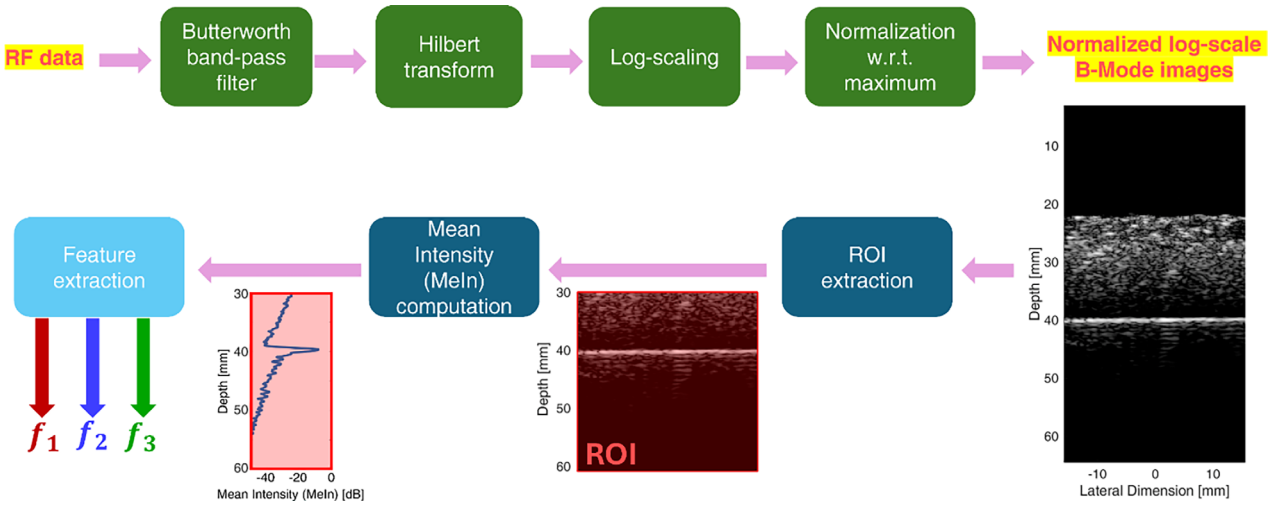

Figure 5. Post-processing pipeline applied to the RF data to extract f_1, f_2, and f_3. Specifically, the green blocks indicate standard post-processing operations applied to the RF data to reconstruct log-scale B-Mode images, whereas the blue blocks indicate the processing operations (applied to the log-scale B-Mode images) utilized to extract f_1, f_2, and f_3. The feature extraction block is colored in light blue, and the specific operations performed inside that block are detailly described in Figure 6.

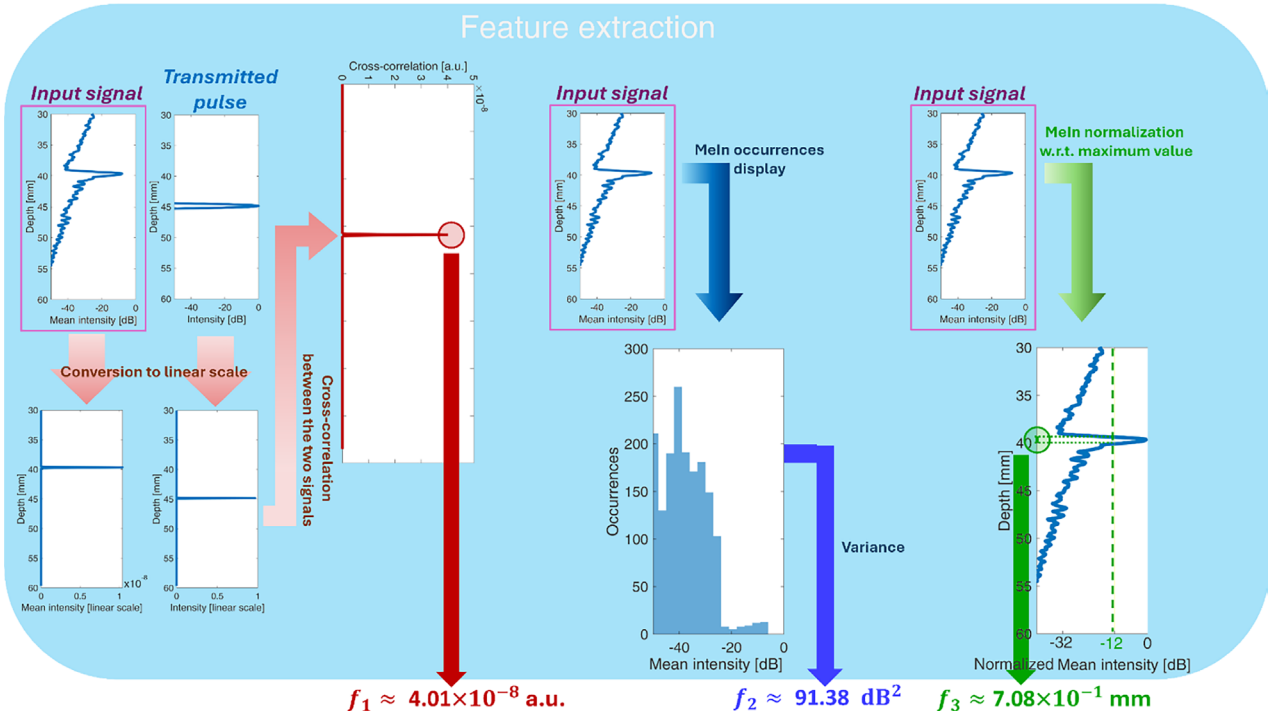

Figure 6. Operations performed inside the feature extraction block are depicted. The example shows how f_1, f_2, and f_3 are obtained from the reconstructed log-scale B-Mode image acquired from *Path 1* with RA=0°.

and dB scale, respectively); (ii) the cross-correlation between the two signals obtained in step (i) was computed; (iii) the maximum of the cross-correlation corresponds to f_1. In this case, it is expected that f_1 increases as the ImP is closer to be perpendicular to the PP (as the MeIn signal is expected to be more similar to the envelope of the transmitted pulse). The extraction of f_2 is particularly straightforward as the distribution of values of the MeIn input signal was directly utilized to extract the MeIn variance, i.e., f_2. Also in this case, it is expected that f_2 increases as the ImP is closer to be perpendicular to the PP. Indeed, as the ImP is closer to be perpendicular to the PP, the distribution of MeIn values is expected to be broader due to the presence also of higher values of MeIn (see, as an example, the presence of values higher than -20 dB in Figure 6). Finally, to extract f_3, the MeIn input signal was normalized with respect to its maximum value, and f_3 computed as the spatial width of the normalized MeIn at -12 dB. Contrary to f_1 and f_2, it is expected that f_3 decreases as the ImP is closer to be perpendicular to the PP. Specifically, given the simplified experimental environment we designed (with a flat steel plate mimicking PP), when the ImP is perpendicular to the PP, it is expected that f_3 is closer to the axial resolution of the system at -12 dB, which should correspond to the width of the transmitted pulse envelope at -12 dB (i.e., $\approx 2.39\times10^{-1}$ mm).

Optimization problems' design

The potential of the above-mentioned features in automatically intercepting the O-ImP was assessed by utilizing GAs. Specifically, f_1, f_2, f_3 were fed to GA_1, GA_2, GA_3, respectively, to solve the following optimization problems to guide UR5e towards the O-ImP:

- GA_1 $\quad max_{pos}\, f_1(pos)$,
- GA_2 $\quad max_{pos}\, f_2(pos)$,
- GA_3 $\quad min_{pos}\, f_3(pos)$,

with *pos* being a position among the 328 explorable positions. Given that the velocity of convergence towards the O-ImP depends on the initialization *pos*, we made 328 runs for each GA. The performance was then evaluated in terms of *"328-runs average angle error (AAE)"*, i.e, the average among the 328 runs of the absolute difference (in degrees °) between the O-ImP and the intercepted ImP as a function of number of explored positions. The utilized GAs were implemented in MATLAB (MathWorks Inc., Natick, USA) with the "*ga*" function, and by setting as optimization options the *"PopulationSize"* and *"EliteCount"* parameters to *2* and *1*, respectively. Therefore, for each run, the utilized GAs start by exploring two different positions. As a next step, the position showing the best value of f_1 (i.e., the maximum), f_2 (i.e., the maximum), and f_3 (i.e., the minimum) for GA_1, GA_2, and GA_3, respectively, will survive and be maintained in the next generation. This process is then repeated until exploring 26 positions. To clarify, following the GA's terminology, each position here corresponds to an *"individual"*.

Additional analysis to test features' combinations

Even though the use of a single feature at a time could be enough to precisely intercept the O-ImP, we also investigated whether a combination of f_1, f_2, and f_3 could improve the performance. However, before combining the features, a proper scaling should be applied to avoid features having a significantly higher absolute value (e.g., f_2) to have an excessively high impact on the maximization problem. To properly apply feature scaling, a further simplified experimental environment (ENV_{NOmeat}) was designed. Specifically, the 2-cm-thick beef meat was removed, and data were acquired and processed to extract the three features as done with ENV_{meat}. To differentiate f_1, f_2, and f_3 (extracted from ENV_{meat}) from the features extracted from ENV_{NOmeat}, we will name the latter as "f_1^{NOmeat}", "f_2^{NOmeat}", and "f_3^{NOmeat}". As f_1, f_2 needed to be maximized, whereas f_3 needed to be minimized, a pre-processing operation was applied to f_3 and f_3^{NOmeat} before scaling. Specifically, we defined

a. $f_3^{mod} = -f_3 + offset$,

b. $f_3^{NOmeat_{mod}} = -f_3^{NOmeat} + offset$,

where *offset* is an arbitrary offset of 1 meter. This operation was necessary to convert the convex shape

of f_3 and f_3^{NOmeat} in a concave shape as f_1, f_1^{NOmeat}, f_2, f_2^{NOmeat}, and thus treating the optimization problem of the combined features as a maximization problem. After this preliminary operation applied to f_3 and f_3^{NOmeat}, scaling was applied as follows:

- $f_1^{scaled}(pos) = \frac{f_1(pos) - min\left(f_1^{NOmeat}\right)}{max\left(f_1^{NOmeat}\right) - min\left(f_1^{NOmeat}\right)}$,
- $f_2^{scaled}(pos) = \frac{f_2(pos) - min\left(f_2^{NOmeat}\right)}{max\left(f_2^{NOmeat}\right) - min\left(f_2^{NOmeat}\right)}$,
- $f_3^{scaled}(pos) = \frac{f_3^{mod}(pos) - min\left(f_3^{NOmeat_{mod}}\right)}{max\left(f_3^{NOmeat_{mod}}\right) - min\left(f_3^{NOmeat_{mod}}\right)}$,

with $min(f_1^{NOmeat})$, $min(f_2^{NOmeat})$, $min(f_3^{NOmeat_{mod}})$ [and $max(f_1^{NOmeat})$, $max(f_2^{NOmeat})$, $max(f_3^{NOmeat_{mod}})$] being the global minima [and maxima] of f_1^{NOmeat}, f_2^{NOmeat}, and $f_3^{NOmeat_{mod}}$, respectively. Then all the possible combinations of f_1^{scaled}, f_2^{scaled}, and f_3^{scaled} were fed to GA_{12}, GA_{13}, GA_{23}, and GA_{123} to solve the following optimization problems to guide UR5e towards the O-ImP:

- $\underline{GA}_{12}$ $max_{pos} ||[f_1^{scaled}(pos), f_2^{scaled}(pos)]||$,
- $\underline{GA}_{13}$ $max_{pos} ||[f_1^{scaled}(pos), f_3^{scaled}(pos)]||$,
- $\underline{GA}_{23}$ $max_{pos} ||[f_2^{scaled}(pos), f_3^{scaled}(pos)]||$,
- $\underline{GA}_{123}$ $max_{pos} ||[f_1^{scaled}(pos), f_2^{scaled}(pos), f_3^{scaled}(pos)]||$,

with $||\bar{v}||$ being the Euclidean norm of a vector $\bar{v}$ (having 2 components when considering GA_{12}, GA_{13}, GA_{23} and 3 components when considering GA_{123}).

Results

Figure 7 shows the 328-runs AAE as a function of number of explored positions for GA_1, GA_2, and GA_3. After exploring 26 positions, the 328-runs AAE is about 0.009°, 1.406°, and 0.070° for GA_1, GA_2, and GA_3, respectively. The strong potential of f_1 and f_3 in automatically intercepting the O-ImP is confirmed when evaluating a 328-runs AAE < 1°. Indeed, in that case, while GA_2 never converges, GA_1 and GA_3 converge after exploring 19 and 18 positions, respectively. A further confirmation on the effectiveness of f_1 and f_3 in automatically intercepting the O-ImP is obtained when evaluating the combination of multiple features (Figure 8). Specifically, after exploring 26 positions, the 328-runs AAE is about 0.082° and 0.095° for GA_{13} and GA_{123}, respectively (i.e., when both f_1^{scaled} and f_3^{scaled} are utilized). In contrast, the 328-runs AAE is higher when only one of those two features is utilized (after exploring 26 positions, the AAE is about 1.168° and 0.131° for GA_{12} and GA_{23}, respectively). Moreover, while GA_{12} is never converging to a 328-runs AAE < 1°, GA_{13}, GA_{23}, and GA_{123} are converging after exploring 18 positions. As a final observation, Figure 9 confirms how, after exploring 26 positions, the use of f_2 (when evaluating GA_2) and f_2^{scaled} (when evaluating GA_{12}) leads to a AAE greater than 12° in 17 and 14 runs over 328 (i.e., 5.2% and 4.3%), respectively. This means that the features based on the variance of MeIn (i.e., f_2 and f_2^{scaled}) present a higher probability in incurring on significantly high errors.

Discussion and conclusions

LUS is an imaging tool widely adopted in the clinical practice. It is however limited by a strong operator dependence in the acquisition and interpretation/analysis processes (4,5). While the operator dependence of the analysis could be mitigated by utilizing automatic and/or quantitative approaches (15–24), the operator dependence of the acquisition could nowadays be reduced only by designing and adopting LUS acquisition protocols (6). However, despite the use of LUS acquisition protocols, HOs can guarantee only a limited precision in intercepting the O-ImP.

Therefore, in this article, we have introduced three features to be utilized to automatically guide a robotic arm (handling an ultrasound probe) towards the O-ImP. It is indeed important to intercept the O-ImP to maximize the intensity at the PP, which is the target of LUS examinations. To further clarify, the transmission of ultrasound pressure along an ImP

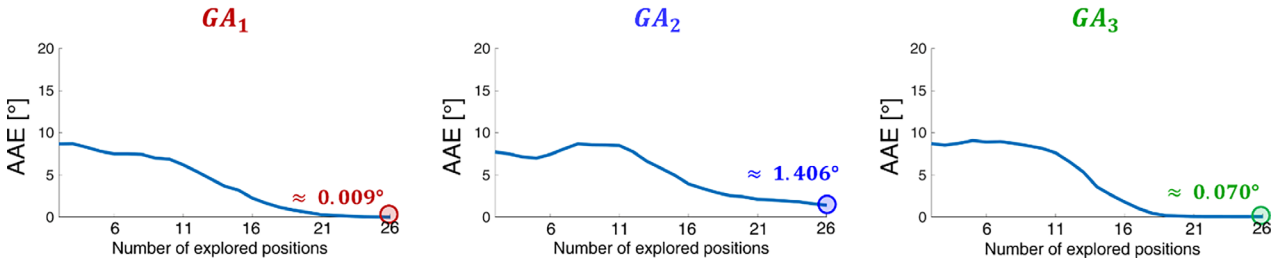

Figure 7. 328-runs AAE as a function of number of explored positions for GA_1, GA_2, and GA_3. The AAEs obtained after exploring 26 positions were also depicted.

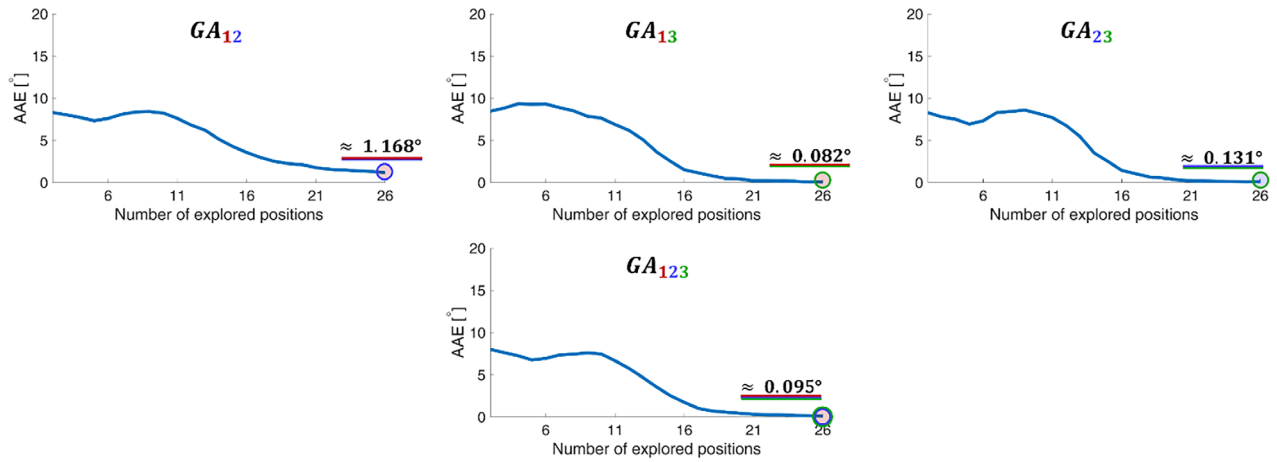

Figure 8. 328-runs AAE as a function of number of explored positions for GA_{12}, GA_{13}, GA_{23}, and GA_{123}. Thus, the first row depicts the results when 2 scaled features are combined, while the second row depicts the results when 3 scaled features are combined. The AAEs obtained after exploring 26 positions were also depicted.

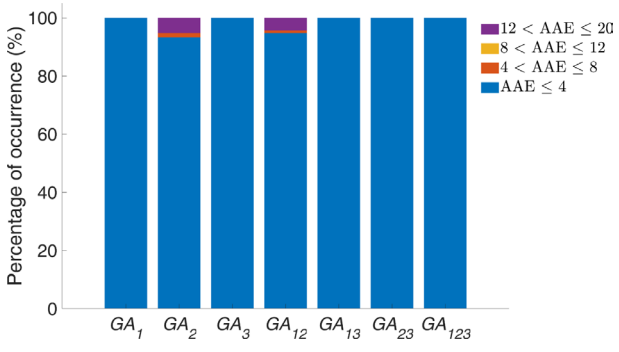

Figure 9. Distribution of 328-runs AAE after exploring 26 positions for GA_1, GA_2, GA_3, GA_{12}, GA_{13}, GA_{23}, and GA_{123}. The values are expressed in terms of percentage of occurrence (%) with respect to the 328 runs.

that is perpendicular to the PP should maximize the received pressure and, thus, allowing a more precise characterization of the PL (thus, indirectly, of the lung surface).

The obtained results show how the evaluated features, especially f_1 and f_3, have a strong potential in automatically intercepting the O-ImP in LUS examinations. Moreover, the results show how the use of multiple features at the same time seems to reduce the capability of the utilized GAs to intercept the O-ImP. However, promising results have been obtained also when combining f_1 and f_3 (the 328-runs AAE is about 0.082° for GA_{13}, which converges to a 328-runs AAE < 1° after exploring 18 positions). Despite the relatively higher 328-runs AAE (after exploring 26 positions) of GA_{13} compared to GA_1 (+0.073°) and GA_3 (+0.012), the use of a combination of features could be motivated by the fact that it may increase the robustness of the approach in a more complex scenario, e.g., in a clinical LUS examination.

The proposed robotic LUS setting is aimed at supporting the automatic interception of the O-ImP.

The proposed approach could be utilized in a semi-supervised LUS exam, in which a human operator (HO) manually places the probe around a specific scanning area and, then, the GAs guide a robotic arm towards the local O-ImP. This would also help limiting the search area of the robot. Even though the proposed robotic LUS setting is aimed at supporting the automatic interception of the O-ImP, potentially, the three proposed features could be utilized as "quality parameters" for a manual scanning performed by a HO. As an example, the HO could start the manual scanning from a point and, while moving towards different directions, check if, e.g., f_1 decreases or increases. This information would alert the HO whether he/she is far or close to the local O-ImP.

In conclusion, it is fundamental to highlight how the GAs here utilized could not represent the best choice for this application but they were chosen to show the potential of the proposed three features (in automatically intercepting the O-ImP), which are indeed the focus of this work.

Moreover, it is important to highlight how the experimental model we utilized is simplified and, thus, could not be able to reflect all the possible aspects present in a real case scenario. As an example, PL is not a "straight" line and it is not necessarily true that PL covers the entire field of view along the lateral dimension. An additional level of complexity in a clinical LUS examination is represented by the motion of the patient, which can introduce a difficulty in guaranteeing the return of the probe to a better position previously found. Furthermore, when considering a pathological lung, the presence of specific LUS imaging patterns as vertical artifacts, consolidations, and pleural effusion could reduce the efficacy of the three proposed features. To mitigate the influence of these imaging patterns to the proposed features, automatic algorithms could be used to detect and segment them (17,22,23,25) before estimating the three proposed features. In this way, these pathological patterns could be removed from the analysis when estimating the MeIn and, consequently, the features' values. It is important to mention that the water/meat acoustic interface is also changing orientation when varying RA, and this can have an impact on the PL intensity. Specifically, the change in orientation of the water/meat acoustic interface causes a change in the direction of propagation of the ultrasound wave before reaching PP, and this could impact on the PL intensity. This scenario is different from a real case scenario, where the contact point with the skin of the patient must be guaranteed and, thus, the water/meat acoustic interface is not present.

As future work, we will explore how these features can be adapted to real case scenarios, where the contact point with the skin of the patient must be guaranteed, and pathological imaging patterns can be present as well as motion of the patient.

Acknowledgements: The authors acknowledge M. Rodriguez for performing the ultrasound data acquisitions, and Dr. E. Lamon and Prof. L. Palopoli for lending the UR5e robot manipulator used during the ultrasound acquisitions.

Author's Contributions: FM analyzed, and interpret the data, and was a major contributor in writing the manuscript. All the authors designed the work, read and approved the final manuscript.

Funding: Part of this work was supported by the Hub Life Science - Advanced Diagnosis (HLS-AD), PNRR PNC-E3-2022-23683266 PNC-HLS-DA, INNOVA – CUP: E63C22003780001, funded by the Italian Ministry of Health under the National Complementary Plan Innovative Health Ecosystem - Unique Investment Code: PNC-E.3.

Availability of Data and Material: The datasets used and/or analyzed during the current study are available from the corresponding author on reasonable request.

Declarations

Ethics Approval and Consent to Participate: N/A.

Consent for publication: N/A.

Competing Interests: The authors declare that they have no competing interests.

References

1. Fatima N, Mento F, Zanforlin A, Smargiassi A, Torri E, Perrone T, et al. Human-to-AI Interrater Agreement for Lung Ultrasound Scoring in COVID-19 Patients. J Ultrasound Med [Internet]. 2023 Apr 1;42(4):843–51. Available from: https://doi.org/10.1002/jum.16052
2. Fatima N, Khan U, Han X, Zannin E, Rigotti C, Cattaneo F, et al. Deep learning approaches for automated classification of neonatal lung ultrasound with assessment of human-to-AI interrater agreement. Comput Biol Med [Internet]. 2024;183:109315. Available from: https://doi.org/10.1016/j.compbiomed.2024.109315
3. Lerchbaumer MH, Lauryn JH, Bachmann U, Enghard P, Fischer T, Grune J, et al. Point-of-care lung ultrasound in COVID-19 patients: inter- and intra-observer agreement in a prospective observational study. Sci Rep [Internet]. 2021;11(1). Available from: https://doi.org/10.1038/s41598-021-90153-2
4. Mento F, Khan U, Faita F, Smargiassi A, Inchingolo R, Perrone T, et al. State of the Art in Lung Ultrasound, Shifting from Qualitative to Quantitative Analyses. Ultrasound Med Biol [Internet]. 2022;48(12):2398–416. Available from: https://doi.org/10.1016/j.ultrasmedbio.2022.07.007
5. Demi L, Wolfram F, Klersy C, De Silvestri A, Ferretti VV, Muller M, et al. New International Guidelines and Consensus on the Use of Lung Ultrasound. J Ultrasound Med [Internet]. 2023 Feb 1;42(2):309–44. Available from: https://doi.org/10.1002/jum.16088
6. Soldati G, Smargiassi A, Inchingolo R, Buonsenso D, Perrone T, Briganti DF, et al. Proposal for International Standardization of the Use of Lung Ultrasound for Patients With COVID-19. J Ultrasound Med [Internet]. 2020;39(7):1413–9. Available from: https://doi.org/10.1002/jum.15285
7. Tsumura R, Hardin JW, Bimbraw K, Grossestreuer A V, Odusanya OS, Zheng Y, et al. Tele-Operative Low-Cost Robotic Lung Ultrasound Scanning Platform for Triage of COVID-19 Patients. IEEE Robot Autom Lett [Internet]. 2021;6(3):4664–71. Available from: https://doi.org/10.1109/lra.2021.3068702
8. Tan J, Li B, Leng Y, Li Y, Peng J, Wu J, et al. Fully Automatic Dual-Probe Lung Ultrasound Scanning Robot for Screening Triage. IEEE Trans Ultrason Ferroelectr Freq Control [Internet]. 2023;70(9):975–88. Available from: https://doi.org/10.1109/tuffc.2022.3211532
9. Lei L, Hu Y, Jiang Z, Miao J, Luo X, Zhang Y, et al. Toward Lung Ultrasound Automation: Fully Autonomous Robotic Longitudinal and Transverse Scans Along Intercostal Spaces. IEEE Trans Med Robot Bionics [Internet]. 2025;7(2):768–81. Available from: https://doi.org/10.1109/TMRB.2025.3550663
10. Mento F, Perini M, Malacarne C, Demi L. Ultrasound multifrequency strategy to estimate the lung surface roughness, in silico and in vitro results. Ultrasonics [Internet]. 2023;135:107143. Available from: https://doi.org/10.1016/j.ultras.2023.107143
11. Blüthgen C, Sanabria S, Frauenfelder T, Klingmüller V, Rominger M. Economical Sponge Phantom for Teaching, Understanding, and Researching A- and B-Line Reverberation Artifacts in Lung Ultrasound. J Ultrasound Med [Internet]. 2017 Oct 1;36(10):2133–42. Available from: https://doi.org/10.1002/jum.14266
12. Mento F, Demi L. On the Influence of Imaging Parameters on Lung Ultrasound B-line Artifacts, in vitro study. J Acoust Soc Am [Internet]. 2020;148(2):975–83. Available from: https://doi.org/10.1121/10.0001797
13. Tortoli P, Bassi L, Boni E, Dallai A, Guidi F, Ricci S. ULA-OP: An Advanced Open Platform for Ultrasound Research. IEEE Trans Ultrason Ferroelectr Freq Control [Internet]. 2009 Oct 1;56:2207–16. Available from: https://doi.org/10.1109/TUFFC.2009.1303
14. Mento F, Soldati G, Prediletto R, Demi M, Demi L. Quantitative Lung Ultrasound Spectroscopy Applied to the Diagnosis of Pulmonary Fibrosis: The First Clinical Study. IEEE Trans Ultrason Ferroelectr Freq Control [Internet]. 2020;67(11):2265–73. Available from: https://doi.org/10.1109/TUFFC.2020.3012289
15. Xue W, Cao C, Liu J, Duan Y, Cao H, Wang J, et al. Modality alignment contrastive learning for severity assessment of COVID-19 from lung ultrasound and clinical information. Med Image Anal [Internet]. 2021;69. Available from: https://doi.org/10.1016/j.media.2021.101975
16. Custode LL, Mento F, Tursi F, Smargiassi A, Inchingolo R, Perrone T, et al. Multi-objective automatic analysis of lung ultrasound data from COVID-19 patients by means of deep learning and decision trees. Appl Soft Comput [Internet]. 2022;109926. Available from: https://doi.org/10.1016/j.asoc.2022.109926
17. Roshankhah R, Karbalaeisadegh Y, Greer H, Mento F, Soldati G, Smargiassi A, et al. Automated segmentation and scoring of lung ultrasound images of COVID-19 patients. J Acoust Soc Am [Internet]. 2020 Oct 1;148(4):2735. Available from: https://doi.org/10.1121/1.5147599
18. Chen J, He C, Yin J, Li J, Duan X, Cao Y, et al. Quantitative Analysis and Automated Lung Ultrasound Scoring for Evaluating COVID-19 Pneumonia with Neural Networks. IEEE Trans Ultrason Ferroelectr Freq Control [Internet]. 2021;68(7):2507–15. Available from: https://doi.org/10.1109/TUFFC.2021.3070696
19. Khan U, Mento F, Giacomaz LN, Trevisan R, Smargiassi A, Inchingolo R, et al. Deep Learning-based Classification of Reduced Lung Ultrasound Data from COVID-19 Patients. IEEE Trans Ultrason Ferroelectr Freq Control [Internet]. 2022;69(5):1661–9. Available from: https://doi.org/10.1109/TUFFC.2022.3161716
20. Khan U, Afrakhteh S, Mento F, Mert G, Smargiassi A, Inchingolo R, et al. Low-complexity lung ultrasound video scoring by means of intensity projection-based video compression. Comput Biol Med [Internet]. 2024;169:107885. Available from: https://doi.org/10.1016/j.compbiomed.2023.107885
21. Khokhlova TD, Thomas GP, Hall J, Steinbock K, Thiel J, Cunitz BW, et al. Development of an Automated

Ultrasound Signal Indicator of Lung Interstitial Syndrome. J Ultrasound Med [Internet]. 2023 Dec 5; Available from: https://doi.org/10.1002/jum.16383

22. Tsai C-H, van der Burgt J, Vukovic D, Kaur N, Demi L, Canty D, et al. Automatic deep learning-based pleural effusion classification in lung ultrasound images for respiratory pathology diagnosis. Phys Medica [Internet]. 2021;83:38–45. Available from: https://doi.org/10.1016/j.ejmp.2021.02.023
23. Roy S, Menapace W, Oei S, Luijten B, Fini E, Saltori C, et al. Deep learning for classification and localization of COVID-19 markers in point-of-care lung ultrasound. IEEE Trans Med Imaging [Internet]. 2020;39(8):2676–87. Available from: https://doi.org/10.1109/TMI.2020.2994459
24. Mento F, Perpenti M, Barcellona G, Perrone T, Demi L. Lung Ultrasound Spectroscopy Applied to the Differential Diagnosis of Pulmonary Diseases: An In Vivo Multicenter Clinical Study. IEEE Trans Ultrason Ferroelectr Freq Control [Internet]. 2024;71(10):1217–32. Available from: https://doi.org/10.1109/TUFFC.2024.3454956
25. Jalilian H, Afrakhteh S, Mento F, Zannin E, Rigotti C, Cattaneo F, et al. Lung ultrasound video scoring using a novel motion-aware segmentation technique: Toward automated neonatal LUS scoring. Comput Biol Med [Internet]. 2025;198:111244. Available from: https://doi.org/10.1016/j.compbiomed.2025.111244